INTERNATIONAL JOURNAL FOR NUMERICAL METHODS IN FLUIDS
Int. J. Numer. Meth. Fluids **30**: 897–919 (1999)

ANALYSIS OF FLUID–STRUCTURE INTERACTION BY AN ARBITRARY LAGRANGIAN–EULERIAN FINITE ELEMENT FORMULATION

P.A. MENDES* AND F.A. BRANCO[1]

Department of Civil Engineering, IST, Av. Rovisco Pais, 1096 Lisboa, Portugal

SUMMARY

In this paper, the interaction fluid–rigid body is analysed by a finite element procedure that incorporates the arbitrary Lagrangian–Eulerian (ALE) method into a well-known two-step projection scheme. The flow is assumed to be two-dimensional, incompressible and viscous, with no turbulence models being included. The flow past a circular cylinder at $\mathscr{R}e = 200$ is first analysed, for fixed and oscillating conditions. The dependence of lock-in upon the shift between the mechanical and the Strouhal frequencies, for a given amplitude of forced vibration, is illustrated. The aerodynamic forces and the wake geometry are compared for locked-in conditions with different driving frequencies. The behaviour of a rectangular cylinder ($B/D = 4$) at $\mathscr{R}e = 500$ (based on height D) is also analysed. The flutter derivatives associated with aerodynamic damping (H_1^* and A_2^* in Scanlan's notation) are evaluated by the free oscillation method for several values of reduced flow speed above the Strouhal one (namely for $3 \leq U^* \leq 8$). Torsional flutter was attained at $U^* \geq 5$, with all the other situations showing stable characteristics. Copyright © 1999 John Wiley & Sons, Ltd.

KEY WORDS: incompressible flow; ALE method; vortex shedding; lock-in; flutter

1. INTRODUCTION

The fluid–structure interaction is an important issue in civil engineering. The design of long-span bridges, high rise buildings, high towers and large domes, for instance, must consider the wind-induced oscillations and the aerodynamic stability has to be properly assured.

In terms of CFD, the arbitrary Lagrangian–Eulerian (ALE) method is a suitable procedure for the analysis of fluid–body interaction. It combines the classical Lagrangian and Eulerian viewpoints and was introduced by Hirt *et al.* [1] in the domain of finite differences, being later developed in the finite element context [2–7]. Besides ALE, other methods can be found in the literature for the analysis of fluid–body interactions, such as those reported in References [8–12].

A CFD program named ESBFI has been developed by the authors for the direct resolution of the Navier–Stokes equations [13]. The ALE method was incorporated into the semi-implicit two-step projection scheme presented by Zienkiewicz *et al.* [14]. In this procedure, the

* Correspondence to: Department of Civil Engineering, IST, Av. Rovisco Pais, 1096 Lisboa, Portugal. Tel.: + 351 1 8418233; fax: + 351 1 8497650; e-mail: mendes@civil.ist.utl.pt
[1] E-mail: fbranco@civil.ist.utl.pt

CCC 0271–2091/99/150897–25$17.50

Received May 1995
Revised August 1995

Taylor–Galerkin method proposed by Donea [15] is applied for the resolution of the intermediate step, and the pressure is evaluated in the projection step by solving a consistent discrete analogue of the Poisson equation for the pressure field.

The immersed bodies are assumed to be rigid and to oscillate with three mechanically uncoupled degrees of freedom. The interaction fluid–moving body is considered through the ALE description, following the format presented by Nomura and Hughes [4]. The spatial domain is divided in two adjacent regions: a fixed outer one, in which the Eulerian description is used, and a moving inner region surrounding the body, in which a compatible mesh velocity field is specified.

The algorithm is applied to the analysis of a circular cylinder at $\mathscr{R}e = 200$, for fixed and oscillating conditions. The results illustrate the dependence of lock-in upon the shift between the mechanical and the Strouhal frequencies, for a peak-to-peak amplitude of forced vibration equal to 20% of the cylinder diameter. The effects of the driving frequency on the aerodynamic forces and on the wake geometry are also illustrated.

The behaviour of a rectangular cylinder with a side ratio depth/height (B/D) equal to 4, at a Reynolds number of 500 ($\mathscr{R}e = UD/\nu$), is also analysed. The expected occurrence of torsional flutter for reduced flow speeds U^* greater than about 4 (where $U^* = U/(f_m \cdot B)$ and f_m is the natural frequency of vibration of the cylinder) was clearly attained in the CFD results.

The evaluation of the flutter derivatives is fundamental for the analysis of the aerodynamic stability of structures, namely for bridge decks. The flutter derivatives of the rectangular section ($B/D = 4$) that are associated with aerodynamic damping (H_1^* and A_2^* in Scanlan's notation) have been evaluated by a CFD simulation of the free oscillation method (FOM). In the past, wind tunnel testing was the only method available to designers, but the results obtained (although still limited to two-dimensional analysis and to low $\mathscr{R}e$, in terms of civil engineering structures) strengthen the belief that CFD will play an important role in the future as an auxiliary tool to civil engineers, particularly in the early stages of design. The geometric definition of the deck of Vasco da Gama Bridge, a cable stayed bridge recently built in Portugal, illustrates the use of CFD as a tool to improve the aerodynamic behavior of structures [16].

2. KINEMATICAL THEORY BEHIND THE ALE DESCRIPTION

Three different domains in space are defined in the ALE description: the spatial domain, the material domain and the referential domain. The spatial domain, $\Omega_x(t)$, is the one in which the fluid flow is currently analysed (at a generic instant t); the current position of the fluid particles are defined by the so called spatial co-ordinates (x_i). The material domain, $\Omega_X(t)$, is defined by the initial position of the fluid particles that constitute Ω_x at time t. The third domain involved in the ALE description is the referential domain ($\Omega\chi$), which is fixed throughout the analysis. For finite element algorithms, Ω_x is simply a moving mesh and $\Omega\chi$ a reference mesh, which may be turned into Ω_x through an adequate mapping.

The velocity vector of a fluid particle (u_i) and the mesh velocity ($\hat{u}_i$) correspond respectively to the material and referential time derivatives of the spatial co-ordinates, i.e.

$$u_i = \left.\frac{\partial x_i}{\partial t}\right|_{X_i = c^{te}}, \tag{1}$$

$$\hat{u}_i = \left.\frac{\partial x_i}{\partial t}\right|_{\chi_i = c^{te}}. \tag{2}$$

In the Eulerian description $\Omega_x = \Omega\chi$ and $\hat{u}_i = 0$; the spatial domain is fixed and each computational element is crossed by the flow. In the Lagrangian description $\Omega_X = \Omega\chi$ and $u_i = \hat{u}_i$; as each element always contains the same fluid particles severe mesh distortions may arise (for instance due to vortex shedding) [3,4].

In the ALE description the nodes of the mesh are free to move independently of the flow, and the mesh distortions can thus be limited. It is a suitable method for the analysis of flow around oscillating rigid bodies, as a purely Eulerian description may be considered in a fixed region of the spatial domain far enough from the immersed body while the compatibility and equilibrium conditions at the moving body–fluid interface are adequately simulated by use of a purely Lagrangian description. A mixed description is used in a transition region, in which a compatible mesh velocity field must be specified.

3. NUMERICAL SOLUTION OF THE NS EQUATIONS

The Navier–Stokes (NS) equations can be written in the following convective–diffusion format (where $i = 1, 2$ and the sum convention on repeated indices is used):

$$\frac{\partial \mathbf{U}}{\partial t} + \frac{\partial \mathbf{F}_i}{\partial x_i} + \frac{\partial \mathbf{G}_i}{\partial x_i} = \mathbf{Q}. \tag{3}$$

In the case of two-dimensional incompressible flow, the vectors introduced above are defined by

$$\mathbf{U} = \rho \begin{bmatrix} u_1 \\ u_2 \end{bmatrix} = \rho \mathbf{V}, \qquad \mathbf{F}_i = \frac{\partial}{\partial x_i} \begin{bmatrix} \rho u_1 (u_i - \hat{u}_i) + P\delta_{1i} \\ \rho u_2 (u_i - \hat{u}_i) + P\delta_{2i} \end{bmatrix}, \qquad \mathbf{G}_i = \begin{bmatrix} -\tau_{1i} \\ -\tau_{2i} \end{bmatrix}, \qquad \mathbf{Q} = \rho \begin{bmatrix} b_1 \\ b_2 \end{bmatrix}, \tag{4}$$

where ρ is the fluid density, P is the pressure, τ_{ij} are the viscous stresses, b_i are the components of gravitational acceleration and δ_{ij} is the Kronecker symbol. The boundary conditions may consist on prescribed velocities ($u_i = \tilde{u}_i$) on a region Γ_u and on prescribed surface tractions ($t_i = \tilde{t}_i$) on a non-overlapping region Γ_t.

The solution of the NS equations is accomplished in the present algorithm by means of the two-step projection semi-implicit scheme presented by Zienkiewicz *et al.* [14]. The system equation (3) is split into

$$\frac{\partial}{\partial t} \Delta\mathbf{U}^* + \frac{\partial \mathbf{F}_i^*}{\partial x_i} + \frac{\partial \mathbf{G}_i}{\partial x_i} = \mathbf{Q}^* \quad \text{(intermediate step)}, \tag{5a}$$

$$\frac{\partial}{\partial t} \Delta\mathbf{U}^{**} + \frac{\partial \mathbf{F}_i^{**}}{\partial x_i} = 0 \quad \text{(projection step)}, \tag{5b}$$

and the integration in time (subscript n refers to the nth time step) is then performed via

$$\mathbf{U}_{n+1} = \mathbf{U}_n + [\Delta\mathbf{U}^*]_n + [\Delta\mathbf{U}^{**}]_n. \tag{6}$$

The expressions (5a) and (5b) are rewritten in the following explicit form, which also defines the vectors introduced above with superscripts (*) and (**),

$$\frac{\partial}{\partial t} \begin{bmatrix} \Delta(\rho u_1)^* \\ \Delta(\rho u_2)^* \end{bmatrix} + \frac{\partial}{\partial x_i} \begin{bmatrix} \rho u_1 (u_i - \hat{u}_i) \\ \rho u_2 (u_i - \hat{u}_i) \end{bmatrix} + \frac{\partial}{\partial x_i} \begin{bmatrix} -\tau_{1i} \\ -\tau_{2i} \end{bmatrix} = \begin{bmatrix} \rho b_1 - \partial P/\partial x_1 \\ \rho b_2 - \partial P/\partial x_2 \end{bmatrix}, \tag{7a}$$

$$\frac{\partial}{\partial t}\begin{bmatrix}\Delta(\rho u_1)^{**}\\ \Delta(\rho u_2)^{**}\end{bmatrix}+\frac{\partial}{\partial x_i}\begin{bmatrix}\Delta P\delta_{1i}\\ \Delta P\delta_{2i}\end{bmatrix}=\begin{bmatrix}\cdot\\ \cdot\end{bmatrix}. \tag{7b}$$

The increment $[\Delta\mathbf{U}^*]_n$ between any consecutive instants is obtained in the intermediate step in order to satisfy equilibrium, assuming that the pressure field $[\mathbf{P}]_n$ evaluated so far is constant during the time step Δt; the increment $[\Delta\mathbf{U}^{**}]_n$ needed to guarantee the continuity condition is then evaluated in the projection step, as well as the corresponding pressure variation $[\Delta\mathbf{P}]_n$, which keeps the equilibrium condition satisfied.

The intermediate step is solved by the following explicit method, which is derived from the Taylor–Galerkin method (TGM) proposed by Donea [15]:

$$[\Delta\mathbf{U}^*]_n=\Delta t\left\{-\frac{\partial\mathbf{F}_i^*}{\partial x_i}-\frac{\partial\mathbf{G}_i}{\partial x_i}+\mathbf{Q}^*+\frac{\Delta t}{2}\left[\frac{\partial}{\partial x_i}\left(\mathbf{A}_i\left(\mathbf{A}_j\frac{\partial\mathbf{U}^*}{\partial x_j}-\mathbf{Q}^*\right)\right)+\frac{\partial\mathbf{Q}^*}{\partial t}\right]\right\}_n. \tag{8}$$

The Jacobian matrices $\mathbf{A}_i$ (note that $i=1, 2$ and that $\mathbf{A}_j$ has been introduced for a sum in indice j) are defined by

$$\mathbf{A}_i=\frac{\partial\mathbf{F}_i^*}{\partial\mathbf{U}}\Leftrightarrow\text{ generic term }(k,m)\text{ of matrix }\mathbf{A}_i,\ (\mathbf{A}_j)_{km}=\frac{\partial(\mathbf{F}_i^*)_k}{\partial\mathbf{U}_m}. \tag{9}$$

The incorporation of the ALE method into this two-step scheme, in conjunction with the transfer of the pressure terms to vector $\mathbf{Q}^*$ (Equation (5a)), leads to the following simple result for the Jacobian matrices

$$\mathbf{A}_1=\begin{bmatrix}2u_1-\hat{u}_1 & 0\\ u_2 & u_1-\hat{u}_1\end{bmatrix},\qquad \mathbf{A}_2=\begin{bmatrix}u_2-\hat{u}_2 & u_1\\ 0 & 2u_2-\hat{u}_2\end{bmatrix}. \tag{10}$$

Besides those contained in $(\partial\mathbf{G}_i/\partial x_i)$, the TGM leads to additional second-order spatial derivatives of the velocity field, which may be interpreted as additional viscous terms. In fact, this procedure is analogous to the upwind schemes of the Petrov–Galerkin streamline balancing type [17–19].

Regarding the projection step, the following implicit procedure ($\gamma\geq 0.5$) is adopted:

$$\rho[\Delta\mathbf{V}^{**}]_n+\gamma\Delta t\nabla[\Delta P]_n=0, \tag{11}$$

where $\nabla=[\partial/\partial x_1,\ \partial/\partial x_2]^T$. The continuity condition ($\nabla^T\mathbf{V}=\mathbf{0}$) is imposed by means of

$$\nabla^T[\mathbf{V}+\gamma\Delta\mathbf{V}^*+\gamma\Delta\mathbf{V}^{**}]_n=0, \tag{12}$$

which in conjunction with (11), leads to the following Poisson equation for the pressures:

$$\gamma^2\Delta t\nabla^2[\Delta P]_n=\rho\nabla^T[\mathbf{V}+\gamma\Delta\mathbf{V}^*]_n. \tag{13}$$

The application of the standard Bubnov–Galerkin weighted residual method gives rise to the expressions given below, where $\mathbf{M}$ is the mass matrix, $\mathbf{K}$ the viscosity matrix, $\mathbf{C}$ the gradient matrix, $\mathbf{S}$ the convection matrix, $\mathbf{H}$ the Laplacian matrix and $\mathbf{F}$ the force vector, and $\mathbf{K}^*$, $\mathbf{C}^*$, $\mathbf{J}^*$ and $\mathbf{F}^*$ correspond to upwind terms. The definitions of these matrices are given in Appendix A.

(1) *Intermediate step*

$$\mathbf{M}[\Delta\mathbf{V}_e^*]_n=[\mathbf{Y}^*]_n,\quad\text{with} \tag{14}$$

$$[\mathbf{Y}^*]_n=\Delta t\left[\mathbf{F}+\mathbf{C}\mathbf{P}_e-\left(\mathbf{K}+\mathbf{S}+\frac{\Delta t}{2}\mathbf{K}^*\right)\mathbf{V}_e+\frac{\Delta t}{2}(\mathbf{F}^*+\mathbf{J}^*-\mathbf{C}^*\mathbf{P}_e)\right]_n. \tag{15}$$

(2) *Projection step*

$$\mathbf{H}[\Delta\mathbf{P}_e]_n = -\frac{\rho}{\Delta t\gamma^2}\mathbf{C}^T[\mathbf{V}_e + \gamma(\Delta\mathbf{V}_e^*)]_n, \tag{16}$$

$$\mathbf{M}[\Delta\mathbf{V}_e^{**}]_n = \gamma\Delta t\mathbf{C}[\Delta\mathbf{P}_e]_n. \tag{17}$$

The Laplacian matrix $\mathbf{H}$ takes its name because it may be interpreted as a discrete counterpart of the Laplacian operator, by analogy with the Poisson equation that must be satisfied by the pressure field in incompressible flows [20]. The matrix $\mathbf{K}$ has an uncoupled format (in terms of u_1 and u_2) as a result of applying the weighted residual formulation to the NS equations with the diffusion term expressed by $\nabla^2 u_i$ rather than in the stress–divergence form [20]. The corresponding natural boundary conditions give rise to surface tractions defined by

$$t_i = \left[\mu\frac{\partial u_i}{\partial x_j} - P\delta_{ij}\right]n_j = \tilde{t}_i \text{ on } \Gamma_t \quad \text{(outlet boundary of the spatial domain)}, \tag{18}$$

where μ is the fluid viscosity and n_i are the components of the unit outward vector normal to the boundary. Although these tractions do not correspond to real physical stresses, this boundary condition is rather efficient for the simulation of outflow surfaces where the mean velocity is normal to the boundary [20–22].

The prescribed values $\tilde{t}_i$ are evaluated by assuming a zero gradient of boundary tractions [14,17,23]. Regarding the prescribed flow velocities, it is convenient to consider two distinct parts in boundary Γ_u—the contour Γ_c of the immersed body, in which the no-slip condition is imposed, and all the remaining portion of Γ_u, which is denoted by Γ_g and consists on the inlet and side boundaries of the domain. Tow-tank conditions are imposed on Γ_g, i.e. $\tilde{u}_1 = U$ (the free flow velocity, which is assumed to be constant along time) and $\tilde{u}_2 = 0$.

The values $\tilde{u}_i$ and $\tilde{t}_i$ are imposed at the intermediate step of the algorithm. At the projection step, both the normal and tangential velocities ($\Delta\mathbf{V}^{**}$) are kept at zero on every point of Γ_u (see Gresho [22] for details about this subject). Even if the prescribed velocities are time-variable (such as on the surface Γ_c of moving bodies, by virtue of the no-slip condition), these velocities are fully imposed at the determination of $\Delta\mathbf{V}^*$.

With respect to the boundary conditions on the pressure field, the equation system (16) presumes that the following conditions are satisfied [14]:

$$\Delta P = 0 \text{ on } \Gamma_t, \qquad \frac{\partial(\Delta P)}{\partial n} = 0 \text{ on } \Gamma_u. \tag{19a, b}$$

The first one is legitimate if the outlet boundary (i.e. Γ_t) is far enough from the immersed bodies [3,24]. It implies that every change on the imposed tractions, during a CFD experiment, must be fully counter-reacted by the viscous component ($\mu\,\partial u_i/\partial n$). The second condition results from (6b) and is a boundary condition usually imposed on Γ_u [3,14,24–26].

The sum of Equations (14) and (17) gives

$$\mathbf{M}[\Delta\mathbf{V}_e]_n = \Delta t[\mathbf{Z}^* + \mathbf{C}(\mathbf{P}_e + \gamma\Delta\mathbf{P}_e)]_n, \tag{20}$$

where

$$[\mathbf{Z}^*]_n = \frac{1}{\Delta t}[\mathbf{Y}^*]_n - [\mathbf{C}\mathbf{P}_e]_n. \tag{21}$$

In the analysis of flows around moving bodies, the matricial blocks corresponding to the ALE portion of the mesh (the region Ω_L defined in Section 4) are time-dependent, as the nodal

co-ordinates are constantly changing. For these conditions, the following procedure, which follows from (20) with $\gamma = 1.0$, has been adopted [13]:

$$\begin{aligned}\mathbf{M}_{n+1}[\mathbf{V}_e]_{n+1} &= \mathbf{M}_n[\mathbf{V}_e]_n + \Delta t\{[\mathbf{Z}^*]_n + \mathbf{C}_n[\mathbf{P}_e]_n + \mathbf{C}_{n+1}[\Delta\mathbf{P}_e]_n\} \\ &= \mathbf{M}_n[\mathbf{V}_e]_n + [\mathbf{Y}^*]_n + \Delta t\mathbf{C}_{n+1}[\Delta\mathbf{P}_e]_n. \end{aligned} \tag{22}$$

The results presented in this paper have been obtained with curved isoparametric finite elements of type $V9/P4$, i.e. biquadratic interpolation for velocity (nine nodes) and bilinear for pressure (four nodes at the vertices). The momentum equations are solved simultaneously and the lumped form of the mass matrix $\mathbf{M}$ has been considered; this procedure shows better stability limits than the use of the consistent mass matrix [17] and the inaccuracies are presumed to be small, as reported by Gresho [21] for elements with biquadratic interpolation for velocity.

4. INTERACTION FLUID–RIGID BODY

The type of spatial domain $\Omega_x(t)$ considered in the analysis is depicted in Figure 1. It is divided in two parts: an inner region $\Omega_L(t)$ with a moving mesh surrounding the immersed body, and a fixed outer region Ω_E in which a purely Eulerian description is considered. The interface between both domains is denoted by Γ_{EL}.

A purely Lagrangian description is used on $\Gamma_c(t)$, with the no-slip condition being imposed by

$$u_i = \hat{u}_i = \tilde{u}_i \quad \text{on } \Gamma_c(t). \tag{23}$$

A rigid immersed body is depicted in Figure 2. The origin of the spatial co-ordinates is located at the centre of gravity of the body (G). The displacements of point G are stored on vector $\mathbf{q} = [X, Y, \alpha]^T$, and the forces induced by the fluid on the body (drag, lift and pitching moment) are stored on vector $\mathbf{X} = [F_D, F_L, M]^T$. These forces are evaluated by

$$F_D = \int_{\Gamma_c} t_1 \, d\Gamma, \qquad F_L = \int_{\Gamma_c} t_2 \, d\Gamma, \qquad M = \int_{\Gamma_c} (t_2 x_1 - t_1 x_2) \, d\Gamma, \tag{24}$$

with

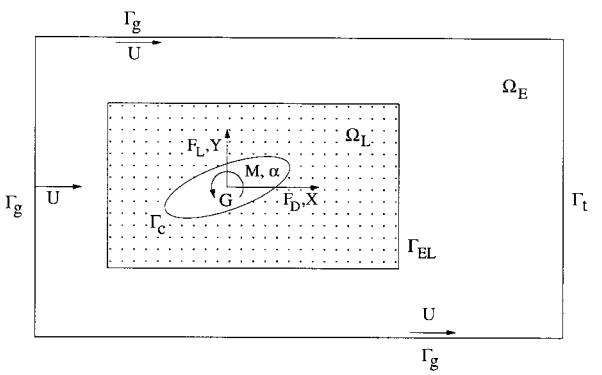

Figure 1. Schematic illustration of the spatial domain.

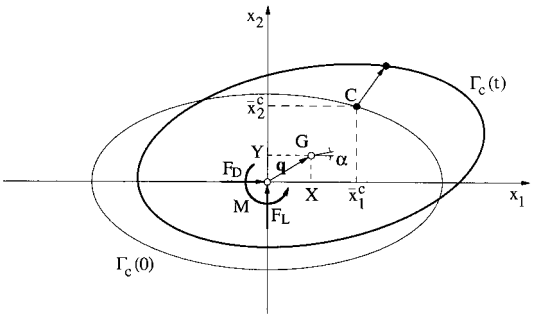

Figure 2. Displacements and forces on the immersed body.

$$t_i = (\tau_{ij} - P\delta_{ij})n_j \Leftrightarrow \begin{cases} t_1 = \mu\left[2\dfrac{\partial u_1}{\partial x_1}n_1 + \left(\dfrac{\partial u_1}{\partial x_2} + \dfrac{\partial u_2}{\partial x_1}\right)n_2\right] - Pn_1 \\ t_2 = \mu\left[\left(\dfrac{\partial u_1}{\partial x_2} + \dfrac{\partial u_2}{\partial x_1}\right)n_1 + 2\dfrac{\partial u_2}{\partial x_2}n_2\right] - Pn_2 \end{cases}. \tag{25}$$

Taking D as a characteristic dimension of the body, the force coefficients are defined by

$$C_D(t) = \frac{F_D(t)}{0.5\rho U^2 D}, \qquad C_L(t) = \frac{F_L(t)}{0.5\rho U^2 D}, \qquad C_M(t) = \frac{M(t)}{0.5\rho U^2 D^2}. \tag{26}$$

For a generic point C of the contour $\Gamma_c(t)$, with initial co-ordinates $\bar{\mathbf{x}} = [\bar{x}_1^c, \bar{x}_2^c]^T$, the relation between its velocity vector $[u_1^c, u_2^c]^T$ and $\dot{\mathbf{q}}$ (the dot indicates $\partial/\partial t$) is as follows [4]:

$$\begin{bmatrix} u_1^c \\ u_2^c \end{bmatrix} = \begin{bmatrix} 1 & 0 & -L_2^c \\ 0 & 1 & L_1^c \end{bmatrix} \begin{bmatrix} \dot{X} \\ \dot{Y} \\ \dot{\alpha} \end{bmatrix} = \mathbf{T}^c\dot{\mathbf{q}}, \tag{27}$$

being $\mathbf{T}^c$ the transformation matrix for point C and

$$\begin{cases} L_1^c = \bar{x}_1^c \cos(\alpha) - \bar{x}_2^c \sin(\alpha) \\ L_2^c = \bar{x}_1^c \sin(\alpha) + \bar{x}_2^c \cos(\alpha) \end{cases}. \tag{28}$$

If the velocities of all the points of $\Gamma_c(t)$ are stored in a vector $\mathbf{V}^c$, then a global transformation matrix $\mathbf{T}$ may be defined such that

$$\mathbf{V}^c = \mathbf{T}\dot{\mathbf{q}} \text{ on } \Gamma_c(t). \tag{29}$$

The mesh velocity field ($\hat{\mathbf{V}}$) may be arbitrarily specified in $\Omega_L(t)$; it only has to satisfy the no-slip condition at the body surface and must be zero at the interface Γ_{EL}, i.e.

$$\begin{cases} \hat{\mathbf{V}} = \mathbf{V}^c & \text{on } \Gamma_c(t) \\ \hat{\mathbf{V}} = 0 & \text{on } \Gamma_{EL} \end{cases}. \tag{30}$$

For each point C of $\Omega_L(t)$ the mesh velocity may thus be specified as a percentage of the velocity that the point would present if it were rigidly linked to the body, i.e.

$$\begin{bmatrix} \hat{u}_1^c \\ \hat{u}_2^c \end{bmatrix} = \kappa^c \begin{bmatrix} 1 & 0 & -L_2^c \\ 0 & 1 & L_1^c \end{bmatrix} \begin{bmatrix} \dot{X} \\ \dot{Y} \\ \dot{\alpha} \end{bmatrix}, \tag{31}$$

with $\kappa^c = 1$ on $\Gamma_c(t)$ and $\kappa^c = 0$ on Γ_{EL}. The simple body geometries that are analysed in the present paper (circular and rectangular cylinders) have enabled the adoption of the same criteria used by Nomura and Hughes [4]—the coefficient κ^c is linearly distributed from 0 to 1 along the line that contains G and each desired node C. This criteria may not be adequate for more complex geometries, but κ^c may then be evaluated by solving the Laplace equation $\nabla^2(\kappa^c) = 0$ on $\Omega_L(t = 0)$ with the boundary conditions stated above.

The rigid body is assumed to behave as a linear oscillator with three mechanically uncoupled degrees of freedom (two linear displacements and rotation), each one characterised by constant mass, viscous damping and stiffness coefficients (denoted by m_i, c_i and k_i respectively, where subscript i corresponds to either X, Y or α).

The step-by-step integration of the equations of motion is performed by the linear acceleration method (LAM). The initial position and velocity of the rigid body must be supplied for the start-up of the oscillation process, and the components of the acceleration vector are evaluated at each step by imposing the condition of dynamic equilibrium

$$\ddot{q}_i(t) = \frac{1}{m_i}\,[X_i(t) - k_i q_i(t) - c_i \dot{q}_i(t)]. \tag{32}$$

5. BASIC EQUATIONS FOR FLUTTER ANALYSIS

In civil engineering, aerodynamic flutter is a major concern on the design of some wind-sensitive structures. Torsional flutter is particularly important in the case of bridge decks, as it is the type of aerodynamic instability more often encountered in wind tunnel tests. The well-known disaster of Tacoma Bridge was attributed to this phenomena.

In its simplest form, the flutter analysis of a cylinder considers only the transverse and the torsional motions. Flutter may then occur with only one degree of freedom being excited or with the simultaneous participation of both. This latter situation is typical of airfoils and is usually termed 'classical flutter'; the former may be of the heaving type (usually termed 'galloping') or of the rotational type, and in both cases the occurrence of flutter corresponds to negative global damping for the corresponding degree of freedom.

Consider a cylinder immersed in a smooth flow with uniform free velocity U, as shown in Figure 3. The equations of dynamic equilibrium between the internal forces and the aerodynamic ones (lift F_L and torsional moment M) are

$$m[\ddot{Y}(t) + 2\xi_{my}\omega_y \dot{Y}(t) + \omega_{my}^2 Y(t)] = F_L(t), \tag{33a}$$

$$I[\ddot{\alpha}(t) + 2\xi_{m\alpha}\omega_\alpha \dot{\alpha}(t) + \omega_{m\alpha}^2 \alpha(t)] = M(t), \tag{33b}$$

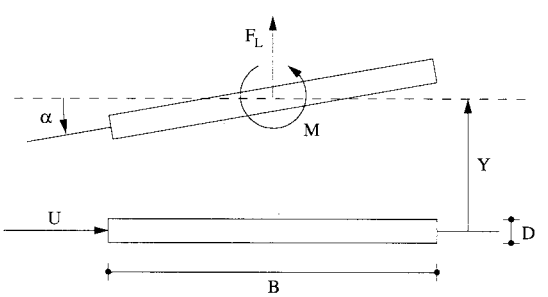

Figure 3. Schematic illustration of an oscillating rectangular cylinder.

where ξ_{my} and $\xi_{m\alpha}$ are the ratio-to-critical structural dampings, ω_{my} and $\omega_{m\alpha}$ are the structural radian frequencies of oscillation ($\omega_m = 2\pi \cdot f_m$), m is the mass of the cylinder per unit length and I is the sectional mass moment of inertia about the rotation axis.

In civil engineering practice, it is usual to adopt Scanlan's notation in the analysis of aerodynamic flutter. The aerodynamic forces are assumed to depend linearly upon the displacements and velocities of oscillation through [27]:

$$F_L(t) = \frac{\rho U^2}{2} B\left[KH_1^*(K)\frac{\dot{Y}(t)}{U} + KH_2^*(K)\frac{B\dot{\alpha}(t)}{U} + K^2H_3^*(K)\alpha(t) + K^2H_4^*(K)\frac{Y(t)}{B}\right],$$

$$M(t) = \frac{\rho U^2}{2} B^2\left[KA_1^*(K)\frac{\dot{Y}(t)}{U} + KA_2^*(K)\frac{B\dot{\alpha}(t)}{U} + K^2A_3^*(K)\alpha(t) + K^2A_4^*(K)\frac{Y(t)}{B}\right], \qquad (34)$$

where the coefficients A_i^* and H_i^* ($i = 1, \ldots, 4$) are called flutter derivatives and $K = 2\pi fB/U$ is the so-called reduced frequency (in this definition, f is the frequency of oscillation). The flutter derivatives H_1^* and A_2^* are related to aerodynamic damping, while the derivatives H_4^* and A_3^* reflect aerodynamic stiffness. The other derivatives play the role of cross-terms between the two degrees of freedom.

The flutter derivatives may be evaluated under forced or free oscillation conditions. In the FOM, the flutter derivatives are evaluated by analysing the motion that is observed after releasing the cylinder from an initial non-zero amplitude. If the rotation is fixed, for example, the net frequency and damping of the transverse oscillations enable to extract H_1^* and H_4^*; similarly, the fixing of the transverse motion leads to A_2^* and A_3^* once the net frequency and damping of the torsional oscillations are evaluated.

In fact, under these experimental conditions, Equations (33) and (34) lead to the following expressions, where the subscript E refers to the values (either of frequency or of damping) that are effectively observed in the tests,

$$H_1^*(K) = \frac{4m}{\rho B^2}\left[\xi_{my}\frac{\omega_{my}}{\omega_{Ey}} - \xi_{Ey}\right], \qquad H_4^*(K) = \frac{2m}{\rho B^2}\left[\left(\frac{\omega_{my}}{\omega_{Ey}}\right)^2 - 1\right], \qquad (35)$$

$$A_2^*(K) = \frac{4I}{\rho B^4}\left[\xi_{m\alpha}\frac{\omega_{m\alpha}}{\omega_{E\alpha}} - \xi_{E\alpha}\right], \qquad A_3^*(K) = \frac{2I}{\rho B^4}\left[\left(\frac{\omega_{m\alpha}}{\omega_{E\alpha}}\right)^2 - 1\right]. \qquad (36)$$

Powerful system identification techniques have been developed for the extraction of the complete set of flutter derivatives. The simple technique described above is used in this paper for the sake of illustration of the CFD potential to assess aerodynamic stability. To this end, only the derivatives associated with one degree of freedom flutter are considered, namely H_1^* (galloping) and A_2^* (torsional flutter).

6. EXAMPLE 1: CIRCULAR CYLINDER AT $\mathscr{R}e = 200$

The flow past a circular cylinder at $\mathscr{R}e = 200$ is first considered for both fixed and forced oscillating conditions. The nature of the flow in forced oscillation conditions at such $\mathscr{R}e$ is essentially two dimensional, as the flow is driven by the oscillations of the cylinder [12]. However, for fixed conditions at $\mathscr{R}e = 200$, the flow in the wake is periodic but in fact it is three-dimensional, as a result of a secondary instability in the two-dimensional vortex street [28]. These three-dimensional effects are not captured in the present analysis.

An overall view of the computational domain is shown in Figure 4. The outflow length is $28D$ and the width of the domain is $16D$. The finite element mesh contains 11958 nodes and

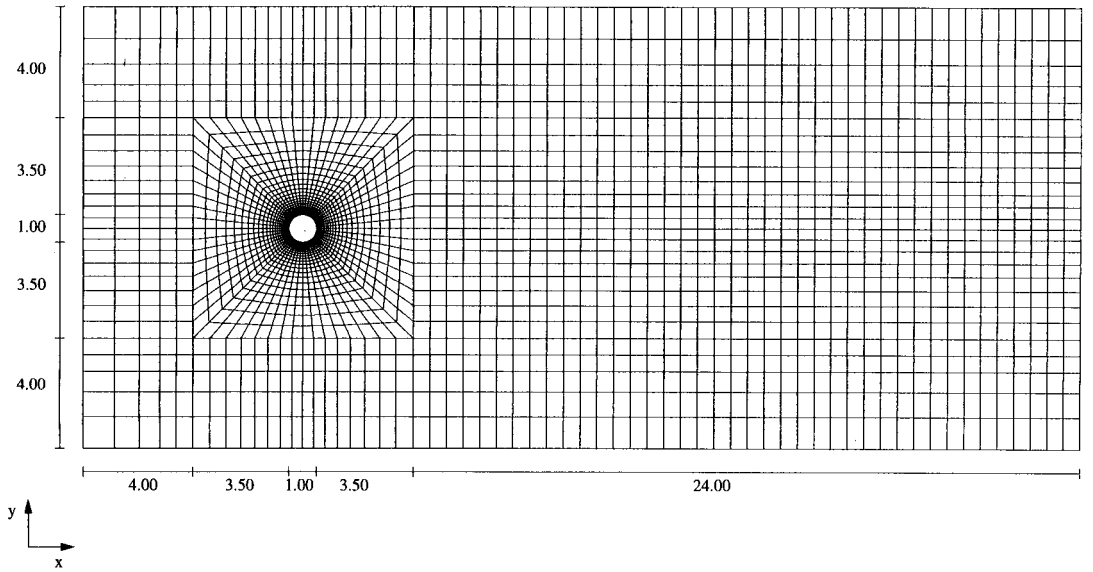

Figure 4. Lay-out of the finite element mesh.

2930 elements, and the Lagrangian region is restricted to a square area centred with the cylinder at rest, with side equal to $8D$. This region contains 25 strips with 64 elements, each one with the minimum radial dimension (the width of the elements that touch the cylinder) being equal to $0.018D$. The dimension of the downstream elements in the direction of the free flow is constant and equal to $0.6D$. This dimension results in about eight elements per the expected wavelength of the vortices shed in stationary conditions, which is about $5D$.

The computations were performed on an IBM-RISC 6000/595, with a non-dimensional time interval $\Delta t^* = \Delta t \cdot U/D = 0.001$ until step 1000 and $\Delta t^* = 0.002$ henceforward. The CPU time per step was 0.40s/0.98s in the simulation of fixed and of oscillating conditions respectively.

6.1. Fixed situation

The frequency of vortex shedding is given by $f_s = (U/D)\mathscr{S}t$, where $\mathscr{S}t$ is the Strouhal number. If for a given frequency f (expressed in cycles per unit of time) a corresponding reduced frequency F is defined by $F = (fD/U)$, the Strouhal number may be viewed as the reduced frequency of vortex shedding (i.e. $\mathscr{S}t = F_s$).

The numerical simulation of vortex shedding may be accomplished by two distinct procedures: by the breakdown of symmetry as a result of the accumulation of round-off errors or by introducing slight perturbations in the numerical process in order to hasten the phenomena. The influence of round-off errors did not prove to be effective and so the authors employed a triggering procedure similar to the one used by Brooks and Hughes [18].

The evolution of the drag and lift coefficients is shown in Figure 5. After an initial stabilisation phase, the fluctuations of the forces show a steady pattern (after time step 30000, approximately), with a reduced frequency $\mathscr{S}t = 0.202$.

As expected, the drag fluctuates with a reduced frequency that is twice the Strouhal number. However, it should be pointed out that the peaks on lift do not occur with simultaneous peaks on drag—a shift of about 108 time steps (i.e. 0.216 units of non-dimensional time) has been observed between a peak on lift and the first subsequent peak on drag. This phase shift is also visible in some published results [29,30].

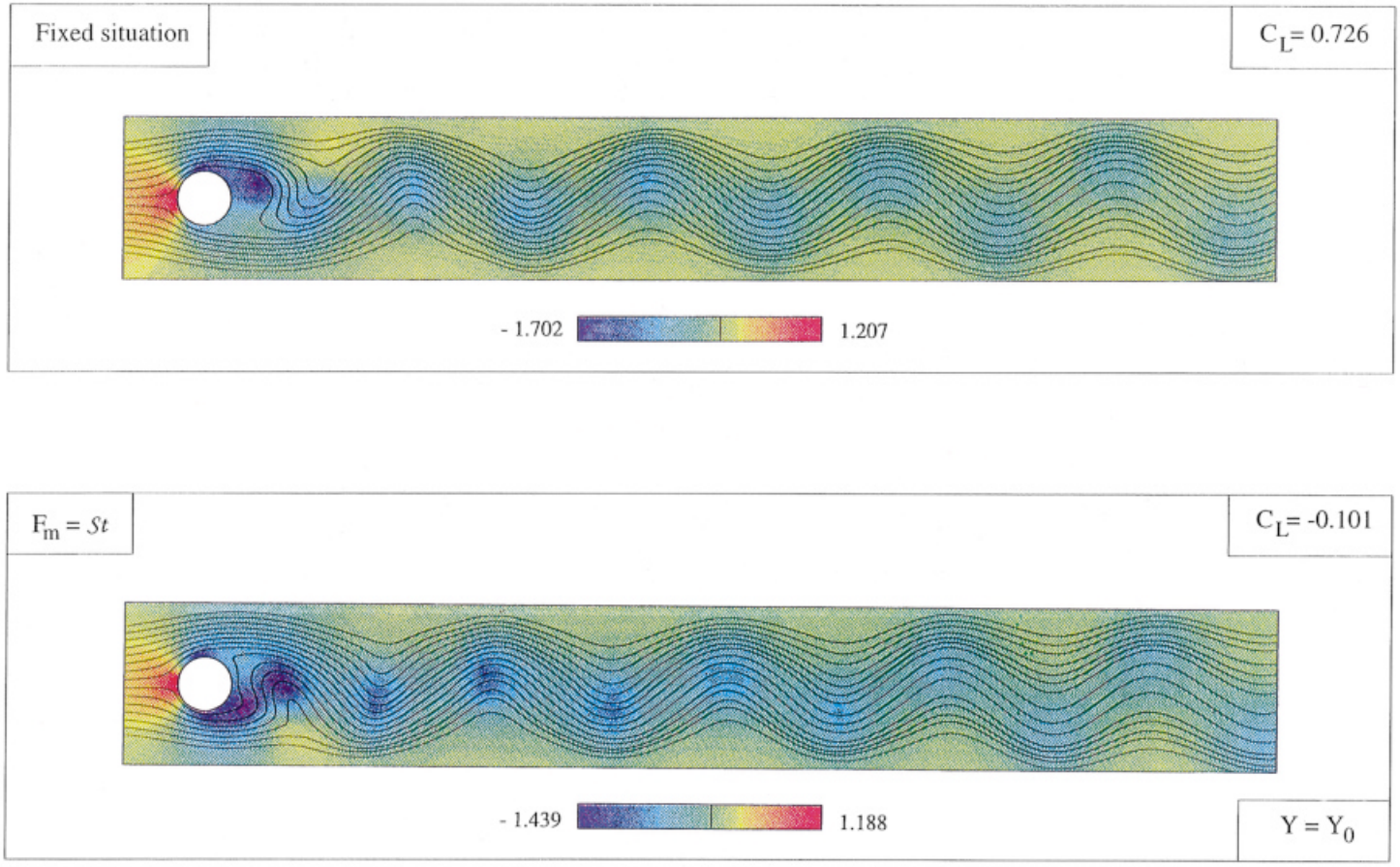

Plate 1. Streamlines and adimensional pressures $P/(0.5\rho U^2)$ in the flow around the cylinder. Upper: fixed situation; lower: $F_m = \mathscr{S}t$.

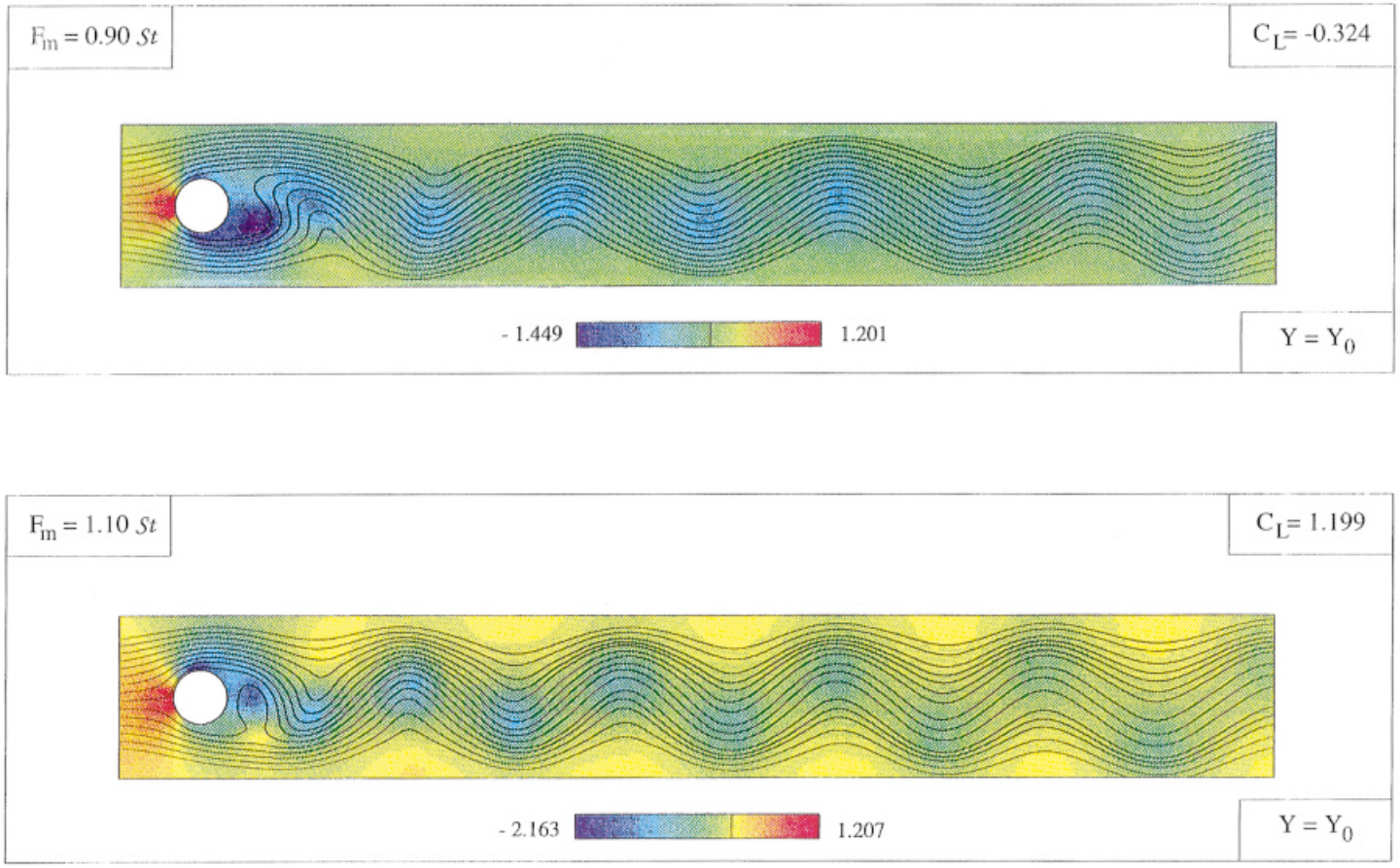

Plate 2. Streamlines and adimensional pressures $P/(0.5\rho U^2)$ in the flow around the cylinder. Upper: $F_m = 0.90\mathscr{S}\ell$; lower: $F_m = 1.10\mathscr{S}\ell$.

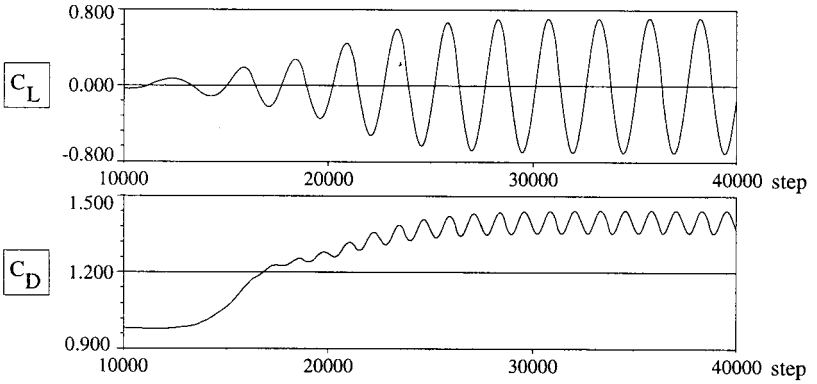

Figure 5. Time series of the force coefficients (steady case, $\mathscr{R}e = 200$, $\Delta t U/D = 0.002$).

The results obtained by the program ESBFI are shown in Table I along with those reported by several other authors, including the Wieselsberger's experimental data as presented by Roshko [31]. Some scatter may be observed, particularly in the force coefficients, but the results of ESBFI are acceptable and no significant blockage effects appear to occur (regarding the value of $\mathscr{S}t$, for instance, the empirical formula of Williamson [32] gives $\mathscr{S}t = 0.197$, which is close to the result of ESBFI).

6.2. *Lock-in under forced vibration conditions*

If a circular cylinder is forced to oscillate transversely, its behaviour is quite dependent upon the ratios Y_0/D and f_m/f_s, where Y_0 and f_m are the (half-)amplitude and frequency of the forced vibration respectively. If the driving frequency is appreciably different from the Strouhal one (f_s), the fluctuations of the fluid dynamic forces show two main components, as the result of the interaction between the cylinder motion and the vortex shedding (which occurs with a frequency f_v close to the steady one, f_s) [36]. The lock-in is the synchronisation of both phenomena and occurs over a limited range of driving frequencies close to f_s, with this frequency range being a function of both $\mathscr{R}e$ and Y_0/D [36,37].

In order to simulate the dependence of lock-in upon the shift between f_m and f_s, under forced vibrations with a given amplitude, and to analyse the effects of the driving frequency on some characteristics of the fluid dynamic forces and wake geometry, four situations with $\mathscr{R}e = 200$ and $Y_0 = 0.10D$ but with different reduced mechanical frequencies have been considered, namely $F_m = 0.90\mathscr{S}t$, $F_m = \mathscr{S}t$, $F_m = 1.10\mathscr{S}t$ and $F_m = 1.20\mathscr{S}t$.

Table I. Force coefficients and Strouhal number (circular cylinder, $\mathscr{R}e = 200$)

Reference	$C_D \pm \Delta C_D$	$\pm \Delta C_L$	$\mathscr{S}t$
ESBFI	1.399 ± 0.049	± 0.726	0.202
Braza *et al.* [33]	1.38	± 0.77	0.20
Zhan and Dalton [12]	1.25 ± 0.03	± 0.54	0.196
Franke *et al.* [34]	1.31	± 0.65	0.194
Lecointe and Piquet [35]	1.46		0.194
Lecointe and Piquet [10]	1.29 ± 0.04	± 0.60	0.195
Wieselsberger (in Roshko [31])	1.38		0.18

According to the experimental results of Koopmann [37], the range frequency for occurrence of lock-in, at $\mathscr{R}e = 200$ and $Y_0 = 0.10D$, is approximately $0.87\mathscr{S}t < F_m < 1.13\mathscr{S}t$. It is thus expected that lock-in occurs in the first three situations, whilst it is not expected to occur in the last one.

The start-up conditions for all the computations correspond to the situation obtained after 30000 time steps with the cylinder fixed in its uppermost position (i.e. at $Y = +Y_0$), with the cylinder being released with zero initial velocity. The sinusoidal motion is imposed by assigning a zero mechanical damping and a high value for the mass parameter $\rho_m = m/(\rho D^2)$, so that the forces induced by the fluid become irrelevant with respect to the mechanical forces developed by the spring. Although this is an approximate procedure, it behaves rather well and does not imply any change in the CFD program. The value $\rho_m = 1000$ proved to be high enough and the stiffness of the spring was evaluated for each case taking into account the value $\mathscr{S}t = 0.202$, which was obtained in the steady situation.

The drag and lift forces obtained in cases $F_m = 1.10\mathscr{S}t$ and $1.20\mathscr{S}t$ are shown in Figures 6 and 7, along with the corresponding power spectral densities (abridged as PSD). The occurrence of lock-in at $F_m = 1.10\mathscr{S}t$ is visible in Figure 6, as C_L and C_D tend to oscillate regularly with reduced frequencies F_m and $2F_m$, while Figure 7 illustrates that lock-in does not occur in the case $F_m = 1.20\mathscr{S}t$. The PSDs obtained at the situations $F_m = 0.90\mathscr{S}t$ and $= 1.00\mathscr{S}t$ are similar to those of $F_m = 1.10\mathscr{S}t$ [13].

In the case of $F_m = 1.20\mathscr{S}t$, the main harmonics of the C_L fluctuations correspond to the reduced frequencies $F_m = 0.242$ and $F_v \approx \mathscr{S}t = 0.202$, while the spectral contents of the C_D fluctuations spread over a wider range of frequencies—the main reduced frequency is $F_1 = (F_m - F_v)$, but some energy may also be attributed to the harmonics with reduced frequency $F_2 = (F_m + F_v)$, $F_3 = (2F_v)$, $F_4 = (2F_v - F_1)$ and $F_5 = (2F_m)$.

In an experiment with forced oscillations of the form $Y(t) = Y_0 \cos(2\pi f_m t)$ and with total duration T, the components of lift that act in phase with the transverse displacement and velocity may be evaluated by [9]

$$C_{LR} = \frac{2}{T}\int_0^T C_L(t)\cos(2\pi f_m t)\,\mathrm{d}t = \frac{2}{(TY_0)}\int_0^T C_L(t)Y(t)\,\mathrm{d}t, \tag{37a}$$

$$C_{LI} = -\frac{2}{T}\int_0^T C_L(t)\sin(2\pi f_m t)\,\mathrm{d}t = \frac{1}{(\pi T f_m Y_0)}\int_0^T C_L(t)\dot{Y}(t)\,\mathrm{d}t. \tag{37b}$$

The imaginary component controls the stability of the cylinder—the condition $C_{LI} > 0$ indicates negative fluid dynamic damping and possible self-excited oscillations, with the cylinder extracting mechanical energy from the flow. This condition is equivalent to $0 < \varphi_L < 180°$, where $\varphi_L = \tan^{-1}(C_{LI}/C_{LR})$ is the angular phase shift between the lift force and the transverse displacement.

The values obtained in each locked-in case for C_{LI} and for φ_L are shown in Table II, along with the lift amplitude C_{L0} defined by

$$C_{L0} = [C_{LR}^2 + C_{LI}^2]^{0.5}. \tag{38}$$

The locked-in situations have negative fluid dynamic damping ($C_{LI} > 0$). The most critical situation in terms of damping is the one with $F_m = \mathscr{S}t$, with the lift force acting almost in phase with the cylinder velocity ($\varphi_L = 95° \approx 90°$) and with the coefficient C_{LI} taking a maximum value ($C_{LI} = 0.762$). The case $F_m = 1.10\mathscr{S}t$ presents the higher C_{L0}, by virtue of a significant value for the component of lift in phase with the transverse displacement (C_{LR}).

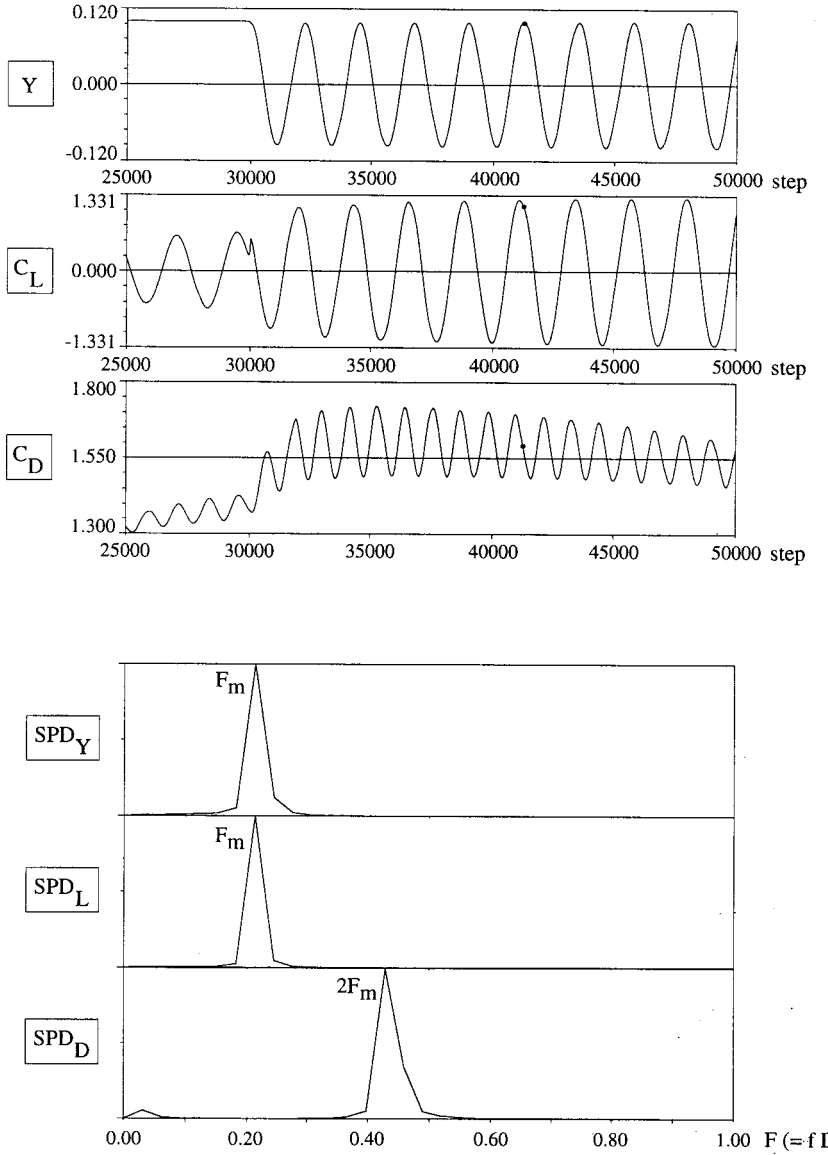

Figure 6. Evolution with time and power spectra of the transverse displacements and force coefficients ($\mathscr{R}e = 200$, $\Delta t U/D = 0.002$, $Y_0/D = 0.10$, $F_m = 1.10\mathscr{S}t$).

With respect to the drag force, the Figure 6 reveals a tendency for a slight increase in the case of $F_m = 1.10\mathscr{S}t$ with respect to the fixed case (although the drag fluctuations are not yet fully established at time step 50000). Among the three locked-in situations, the case $F_m = \mathscr{S}t$ presented the higher mean value ($C_D \approx 1.53$) and also the higher amplitude of fluctuation of the drag force [13].

Some similar results have been obtained by other authors—Chilukury [9], for instance, reports $C_{LI} \approx 0.62$ for $\mathscr{R}e = 144$, $F_m = \mathscr{S}t$ and $Y_0/D = 0.14$, and also indicates, for $\mathscr{R}e = 80$ and $Y_0/D = 0.14$, a slight increase in drag for $F_m = \mathscr{S}t$ (about 12% with respect to the steady case), while no drag amplification has been attained in other oscillating cases with F_m close to $\mathscr{S}t$.

Other CFD results are those of Hurlbut *et al.* [8]—for $\mathscr{R}e = 80$ and $Y_0/D = 0.14$, the values $[C_{LI} \approx 0.35,\ \varphi_L \approx 93°]$ are reported for $F_m = \mathscr{S}t$ $(= 0.16)$, and $[C_{LI} \approx 0.10,\ \varphi_L \approx 157°]$ for $F_m = 0.875\mathscr{S}t$ $(= 0.14)$. These values agree with the experimental ones obtained by Tanida *et al.* [36] for the same $\mathscr{R}e$ $(= 80)$. However, the drag amplification observed by Tanida *et al.* in locked-in conditions is higher than the one obtained via CFD [8,9].

The results obtained by the authors also indicate that both the mean drag and the imaginary component of the lift coefficient attain maximum values at $F_m = \mathscr{S}t$. The values obtained in this situation for the drag amplification and for the phase shift between lift and motion are similar to the CFD results reported by Hurlbut *et al.* [8] and by Chilukuri [9].

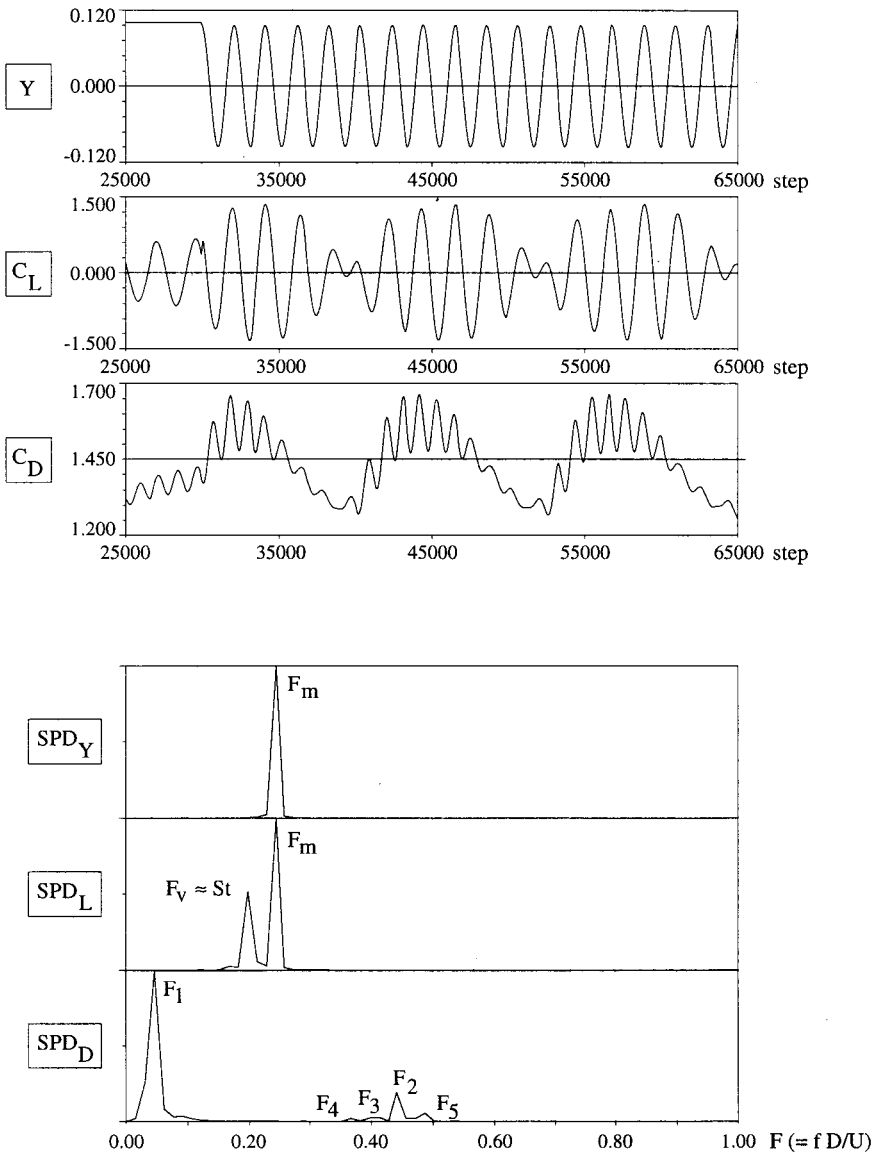

Figure 7. Evolution with time and power spectra of the transverse displacements and force coefficients ($\mathscr{R}e = 200$, $\Delta t U/D = 0.002$, $Y_0/D = 0.10$, $F_m = 1.20\mathscr{S}t$).

Table II. Properties of the lift force in the locked-in situations

	$F_m = 0.90\mathscr{S}t$	$F_m = \mathscr{S}t$	$F_m = 1.10\mathscr{S}t$
C_{LI}	0.193	0.762	0.481
C_{L0}	0.402	0.765	1.293
φ_{L} (°)	151	95	22

In order to investigate the influence of the driving frequency on the spacing of the vortices in the wake at locked-in conditions, and to compare it with the fixed situation, the streamlines and the fluid pressures obtained near the cylinder at an instant of maximum upwards lift in the fixed case and at instants of uppermost position in the oscillating cases are plotted in Plates 1 and 2. This instant is identified by a small dot in Figure 6 for the case $F_m = 1.10\mathscr{S}t$.

The pressure scales in the plates vary from case to case, but always range from dark red (higher pressures) to dark blue (lower ones). The blue zones in the downstream wake of the cylinder correspond to the instantaneous location of the shed vortices.

The following conclusions may be drawn from this figure:

- The longitudinal and lateral spacing between the vortices in the wake are similar in the fixed situation and in the case of $F_m = \mathscr{S}t$. The experimental results obtained by Koopmann [37] and Griffin *et al.* [38] for similar $\mathscr{R}e$ illustrate this property for the longitudinal spacing but also report a slight decrease in the lateral spacing, which is not visible in the CFD results;
- The downstream wake in the case of $F_m = 0.90\mathscr{S}t$ is more regular than in the case of $F_m = 1.10\mathscr{S}t$, which was also experimentally observed [37,38];
- The longitudinal vortex spacing varies inversely with the vibration frequency; the lateral spacing changes little with this parameter, but a slight tendency to decrease for frequencies lower than the Strouhal one may be noticed. These properties are in agreement with the experimental results [37,38].

7. EXAMPLE 2: RECTANGULAR CYLINDER AT $\mathscr{R}e = 500$

The flow around a rectangular section with a side ratio $B/D = 4$ at a Reynolds number of 500 (based on height D, i.e. $\mathscr{R}e = UD/\nu$) was analysed for both fixed and oscillating conditions. This section was chosen because it enables the illustration of the CFD potential in the assessment of aerodynamic stability of structures.

In fact, wind tunnel tests reveal that this section is prone to torsional flutter, which is a phenomenon often encountered in testing bridge decks. The value of $\mathscr{R}e = 500$ was adopted because it is attainable (with program ESBFI and with the hardware available) with a reasonable computer runtime and because there exist in the literature several CFD analysis of this section at such $\mathscr{R}e$ and for fixed conditions (Okajima [23] and Okajima *et al.* [39,40]).

The finite element mesh used in this study is shown in Figure 8. It contains 18 528 nodes and 4532 elements, and the Lagrangian region is a rectangle ($8D$ per $4D$) centred with the cylinder at rest. The elements that touch the cylinder have a dimension normal to the surface equal to $0.025D$ and a tangential dimension varying between $0.025D$ at the corners and $0.12D$ at the middle of each side. The CPU time per step (on an IBM-RISC 6000/595) was 0.65s/1.47s in the simulation of fixed and of oscillating conditions respectively.

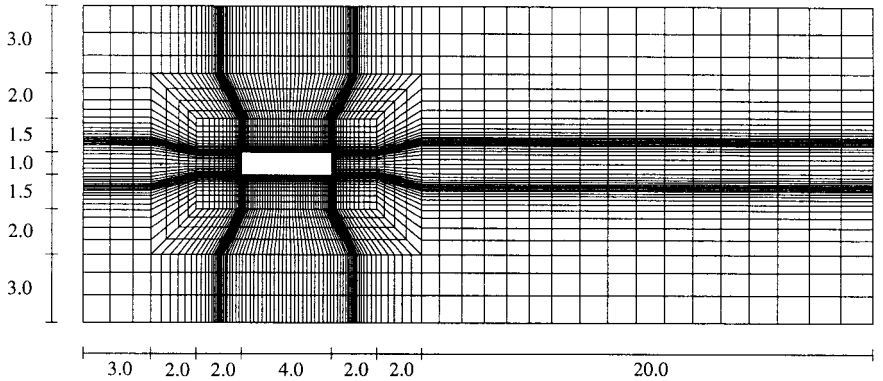

Figure 8. Layout of the finite element mesh.

7.1. Fixed conditions

The flow was first analysed for fixed conditions, with the occurrence of vortex shedding being hastened by the perturbation technique referred to above. The evolution of the drag, lift and moment coefficients is shown in Figure 9. After an initial stabilisation phase, these force coefficients oscillate regularly as a result of alternate vortex shedding.

The values obtained for the average C_D, for the (half-)amplitude of C_L and for $\mathscr{S}t$ are shown in Table III along with the CFD results reported by Okajima [23] for the same $\mathscr{R}e$ (these values of C_D and of ΔC_L are only approximate, as they were taken from figures; besides, the value $\Delta C_L \approx 1.85$ attributed to Okajima [23] is half of the peak-to-peak amplitude of the lift fluctuations presented therein, which are rather regular but do not present zero mean).

The distribution of the flow velocities in the vicinity of the rectangular section at an instant with maximum upwards lift, at the first instant of zero lift that occurs afterwards and at the following instant with maximum downwards lift are shown in Figure 10. These selected instants are the ones marked with a dark square in Figure 9. Clearly visible are the

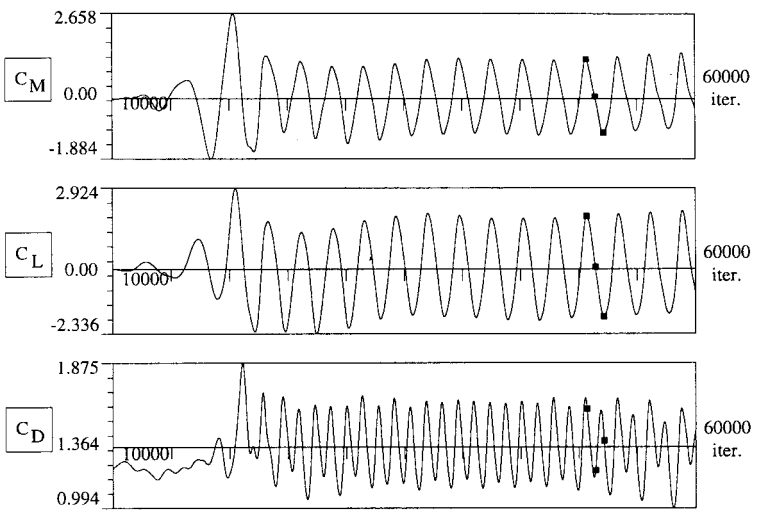

Figure 9. Evolution with time of the force coefficients ($\mathscr{R}e = 500$, $\Delta t U/D = 0.00244$).

Table III. Force coefficients and Strouhal number (rectangular section, $B/D = 4$, $\mathscr{R}e = 500$)

Reference	C_D	ΔC_L	$\mathscr{S}t$
ESBFI	1.364	± 2.00	0.149
Okajima [23]	1.35	± 1.85	0.13

reattachment on the lateral sides of the separation surface that is created at the frontal corners, as well as the vortices near the rear corners and in the wake. The flow patterns shown in Figure 10 are similar to those presented by Okajima [23] and by Okajima *et al.* [39,40].

7.2. Evaluation of flutter derivatives

As mentioned by Nakamura and Yoshimura [41], the onset of torsional flutter at high flow speeds is related to the reattachment of the shear layers separated at the leading edge and to its interaction with the structural motion (fluid memory effect). Rectangular sections with ratio B/D less than 2.5 or greater than 5.5 are not prone to torsional flutter, the former because the

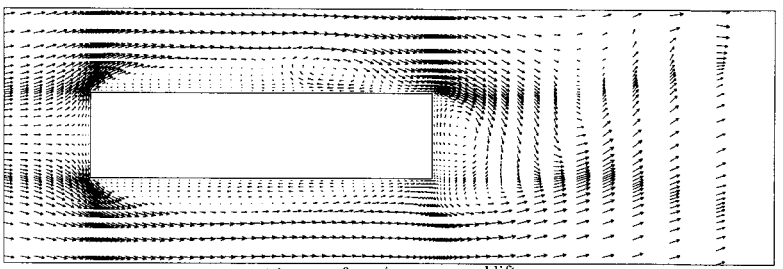

a) instant of maximum upward lift.

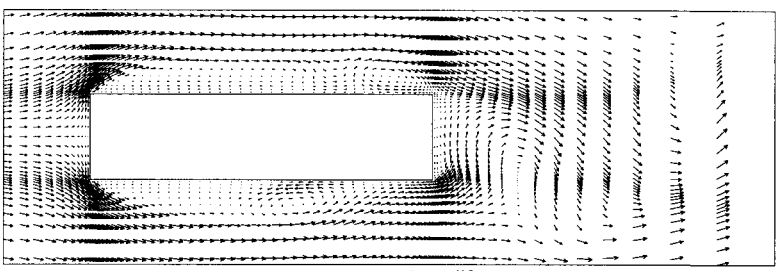

b) instant of zero lift.

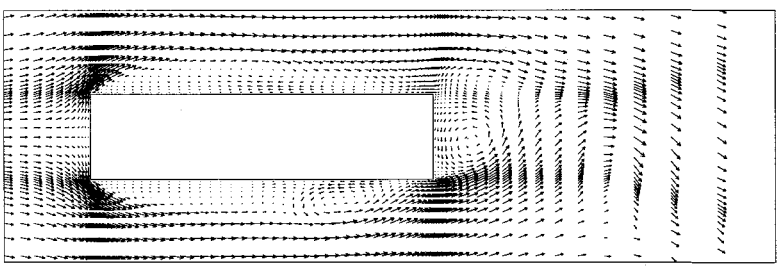

c) instant of maximum downward lift.

Figure 10. Velocity field near the section in the fixed situation ($\mathscr{R}e = UD/v = 500$).

flow is fully separated along the lateral sides (which makes them more sensible to galloping) and the latter because the separation bubbles near the leading edge corners are too short to affect strongly the way how the pressure field on the cylinder surface adapts to changes of position due to the rigid body motion.

Wind tunnel tests on a rectangular section with $B/D = 4$ indicate that the aerodynamic torsional damping becomes negative for reduced flow speeds, $U^* = U/(f_m B)$, greater than about 4 (Nakamura *et al.* [41], Washizu *et al.* [42], Nakamura [43], Huston [44]).

These wind tunnel tests were performed at $\mathscr{R}e \approx 10^4$–$10^5$, which is a value not attainable with the program ESBFI and the hardware available. However, the analysis of the fluid–structure interaction at the same $\mathscr{R}e$ that was considered in the steady case, namely $\mathscr{R}e = 500$, can be performed with a reasonable computational effort (the evaluation of 70000 steps under oscillating conditions, such as was performed for case $U^* = 8$, takes 29 h of CPU in the computer referred to above). The CFD results shown in the following illustrate the dependence of stability upon U^* at $\mathscr{R}e = 500$ with emphasis on the torsional behaviour—the torsional oscillations were studied for $U^* = 3$, 5, 6 and 8, while the transverse oscillations were studied only for $U^* = 3$ and 8.

Sections with sharp corners are less sensitive to $\mathscr{R}e$ effects than, for instance, circular sections. Based on wind tunnel tests of this rectangular section at $\mathscr{R}e$ much higher than 500, Washizu *et al.* [45] report the values $C_D \approx 1.20$ and $\mathscr{S}t \approx 0.13$, which are close to the CFD results at $\mathscr{R}e \approx 500$. Thus, if in fact the $\mathscr{R}e$ effects are not pronounced, it is expected that the CFD analyses at $\mathscr{R}e \approx 500$ also reveal a stable behaviour in torsion at $U^* = 3$ and unstable at $U^* = 8$. With respect to the transverse oscillations, stable conditions are expected to occur for the range of U^* considered ($3 \leq U^* \leq 8$), since this section is not prone to galloping at such flow speeds [45,46]. In fact, if the value $\mathscr{S}t = 0.149$ is considered (vd. Table III), the reduced Strouhal flow speed may be estimated as $U_s^* = U/(f_s B) = D/(B\mathscr{S}t) \approx 1.68$, which is below the range of U^* considered in the CFD analysis.

The flutter derivatives associated with flutter on a single degree of freedom (H_1^* and A_2^*) were evaluated by a CFD simulation of the FOM. The torsional and transverse oscillations were studied in separate, with the longitudinal motion being fixed. All the computations were carried out with zero structural damping, with the body motion starting after 30000 time steps with the cylinder fixed on its initial position (Y_0 or α_0).

The initial amplitude of each motion is equal for every U^*, namely $\alpha_0 = 1.8°$ and $Y_0 = 0.16D$. These values are similar to those adopted in wind tunnel tests (for instance, Nakamura and Yoshimura [41], Nakamura and Mizota [46]). As the structural damping is zero on the CFD experiments, the observed effective damping is equal to the aerodynamic one and the flutter derivatives are simply obtained by

$$H_1^* = -\frac{m}{\rho B^2}\frac{2\delta_{Ey}}{\pi}, \qquad A_2^* = -\frac{I}{\rho B^4}\frac{2\delta_{E\alpha}}{\pi}, \tag{39}$$

where δ_E ($\approx 2\pi \cdot \xi_E$) is the average logarithmic decrement of the oscillations. As the flutter derivatives do not depend on the mass parameters $\rho_m = m/(\rho B^2)$ and $\rho_I = I/(\rho B^4)$, these equations show that the effective damping is inversely proportional to them. Thus, it is convenient to consider low values of these parameters in the CFD experiments, in order to extract meaningful results with few cycles of oscillation (i.e. with less demand of CPU).

The evolution of the displacements and of the forces is shown in Figures 11 and 12 for $U^* = 3$ and for $U^* = 8$. Regarding the transverse oscillations, stable conditions have been obtained in both cases. With respect to the torsional oscillations, case $U^* = 3$ is stable and case $U^* = 8$ is unstable, with growing amplitudes revealing the occurrence of torsional flutter. This behaviour is similar to the one observed in the wind tunnel tests.

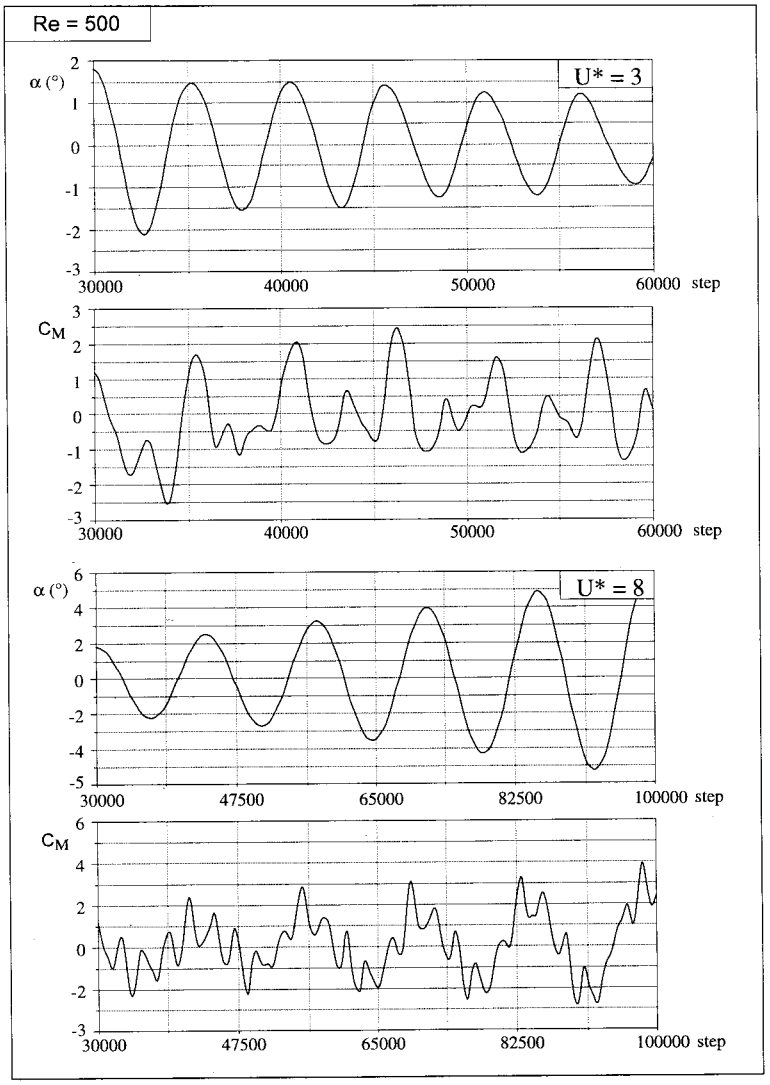

Figure 11. Evolution of rotation and of moment coefficient ($\alpha_0 = 1.8°$, $\Delta t U/D = 0.00244$).

The results obtained for the flutter derivatives (H_1^* and A_2^*) are presented in Table IV. The positive values indicate unstable conditions. Figure 13 illustrates the values of A_2^* obtained via CFD and those reported by Huston [44] and by Nakamura and Yoshimura [41] based on wind tunnel experiments under free oscillation conditions and smooth flow (these experimental values are approximate, since they were extracted from figures). Some scatter may be observed, even between the wind tunnel results themselves, but the CFD results are on the trend.

With respect to the transverse oscillations, Shangpei and Xin [47] have performed tests under free oscillation conditions and report H_1^* $(U^* = 3) \approx -1.0$ and H_1^* $(U^* = 8) \approx -5.0$ for a section not exactly rectangular but rather trapezoidal with $B_{\text{upper}}/D = 4$ and $B_{\text{lower}}/D = 3.33$. As for the torsional case, the results obtained via CFD for the transverse oscillations agree with what might be expected, as they reveal stable conditions for both values of U^* and this characteristic becomes more pronounced for $U^* = 8$.

8. CONCLUSIONS

The ALE description has been successfully incorporated in a well-known two-step projection scheme for the resolution of NS equations. The occurrence of lock-in is investigated for a circular cylinder at $\mathscr{R}e = 200$, under forced transverse vibrations with a peak-to-peak amplitude equal to 20% of the diameter. The results illustrate the influence of the driving frequency at locked-in conditions on some characteristics of the aerodynamic forces and of the wake geometry, such as the mean drag and lift amplitude, the spacing between the vortices in the wake and the phase shift lift motion. The behaviour of a rectangular section with a side ratio $B/D = 4$, at $\mathscr{R}e = UD/v = 500$, has also been analysed via CFD. The flutter derivatives H_1^* and A_2^* were evaluated by the FOM for values of the reduced flow speed in the range $3 \leq U^* \leq 8$.

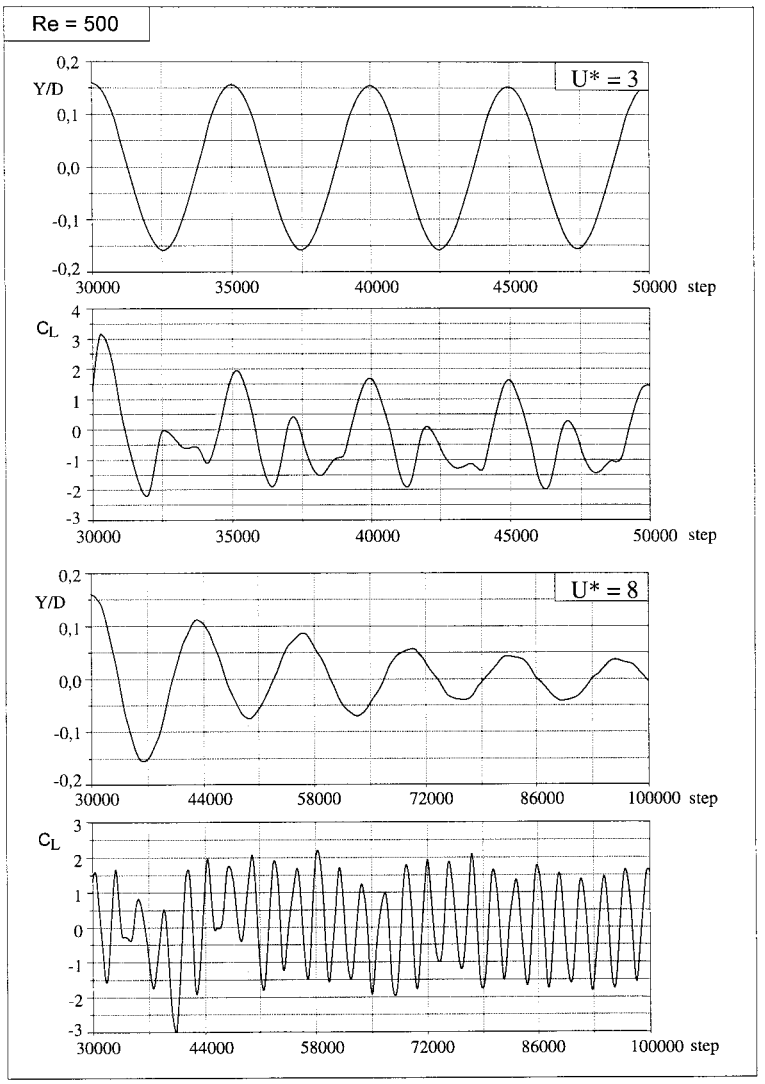

Figure 12. Evolution of transverse displacement and of lift coefficient ($Y_0 = 0.16D$, $\Delta tU/D = 0.00244$).

Table IV. CFD results for the aerodynamic damping and for the flutter derivatives

U^*	H_1^*	A_2^*
3	−0.224	−0.102
5	—	0.175
6	—	0.477
8	−5.600	1.525

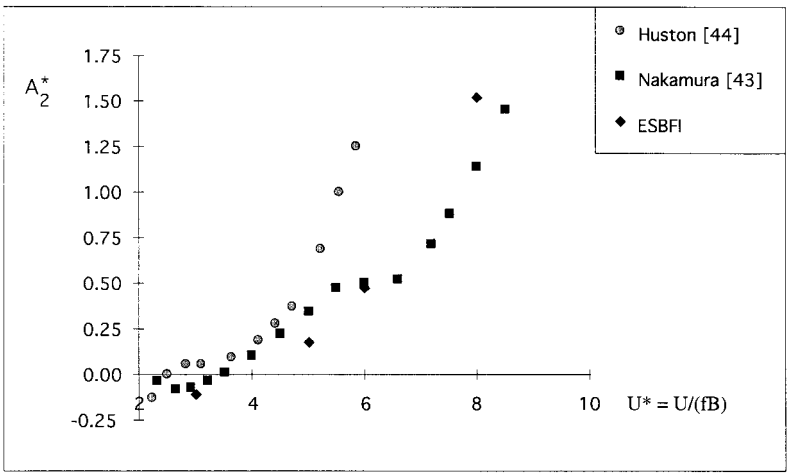

Figure 13. Flutter derivative A_2^*—experimental and CFD results.

With respect to torsional oscillations, a negative value of the fluid dynamic damping has been obtained in cases with $U^* \geq 5$. The transverse oscillations have shown stable characteristics for every U^* in the range considered. Despite the low $\mathscr{R}e$ considered and the two-dimensional hypothesis, the results are encouraging in terms of future application of CFD to the design of wind-sensitive structures, as an auxiliary tool to wind tunnel tests.

APPENDIX A. DEFINITION OF ELEMENTARY MATRICES

At an elementary level (i.e. before the assembling process), the matrices introduced in Equations (14)–(17) are defined by the following expressions (the sum convention on repeated indices is used):

$$\text{Mass matrix:} \quad \mathbf{M} = \begin{bmatrix} \mathbf{M1} & \cdot \\ \cdot & \mathbf{M1} \end{bmatrix} \quad \text{with} \quad \mathbf{M1}_{ij} = \rho \delta_{ij} \int_{\vartheta} N_i^v \, \mathrm{d}\vartheta,$$

$$\text{Viscosity matrix:} \quad \mathbf{K} = \begin{bmatrix} \mathbf{K1} & \cdot \\ \cdot & \mathbf{K1} \end{bmatrix} \quad \text{with} \quad \mathbf{K1}_{ij} = \mu \int_{\vartheta} \frac{\partial N_i^v}{\partial x_k} \frac{\partial N_j^v}{\partial x_k} \, \mathrm{d}\vartheta,$$

$$\text{Gradient matrix:} \quad \mathbf{C} = \begin{bmatrix} \mathbf{C}_1 \\ \mathbf{C}_2 \end{bmatrix} \quad \text{with} \quad (\mathbf{C}_m)_{ij} = \int_{\vartheta} \frac{\partial N_i^v}{\partial x_m} N_j^p \, \mathrm{d}\vartheta \quad (m = 1, 2),$$

Convextion matrix: $\mathbf{S} = \begin{bmatrix} \mathbf{S1} & \cdot \\ \cdot & \mathbf{S1} \end{bmatrix}$ with $\mathbf{S1}_{ij} = \rho(u_{mk} - \hat{u}_{mk})\mathbf{S2}_{ijmk}$ and

$$\mathbf{S2}_{ijmk} = \int_{\vartheta} N_i^v N_k^v \frac{\partial N_j^v}{\partial x_m} \, \mathrm{d}\vartheta,$$

Force vector: $$\mathbf{F} = \rho \int_{\vartheta} [(\mathbf{N}^v)^T \mathbf{b}] \, \mathrm{d}\vartheta + \int_{\Gamma_t} [(\mathbf{N}^v)^T \tilde{\mathbf{t}}] \, \mathrm{d}\Gamma,$$

Laplacian matrix: $$\mathbf{H}_{ij} = \int_{\vartheta} \left[\frac{\partial N_i^p}{\partial x_1} \frac{\partial N_j^p}{\partial x_1} + \frac{\partial N_i^p}{\partial x_2} \frac{\partial N_j^p}{\partial x_2} \right] \mathrm{d}\vartheta,$$

$$\mathbf{K}^* = \rho \int_{\vartheta} \frac{\partial (\mathbf{N}^v)^T}{\partial x_i} \mathbf{A}_i \mathbf{A}_j \frac{\partial \mathbf{N}^v}{\partial x_j} \, \mathrm{d}\vartheta, \qquad \mathbf{C}^* = \int_{\vartheta} \frac{\partial (\mathbf{N}^v)^T}{\partial x_i} \mathbf{A}_i (\nabla \mathbf{N}^p) \, \mathrm{d}\vartheta,$$

$$\mathbf{F}^* = \int_{\Gamma_t} (\mathbf{N}^v)^T \frac{\partial}{\partial t} \begin{bmatrix} \rho u_1 (u_n - \hat{u}_n) \\ \rho u_2 (u_n - \hat{u}_n) \end{bmatrix} \mathrm{d}\Gamma, \qquad \mathbf{J}^* = \int_{\vartheta} \frac{\partial (\mathbf{N}^v)^T}{\partial x_i} \mathbf{A}_i \rho \mathbf{b} \, \mathrm{d}\vartheta.$$

In these expressions, ϑ is the elementary domain, u_{mk} is the mth component of velocity ($m = 1, 2$) at the kth velocity node of the element ($k = 1, \ldots, 9$ for biquadratic interpolation), u_n is the normal component of velocity at Γ_t, $\mathbf{b} = [b_1, b_2]^T$, $\tilde{\mathbf{t}} = [\tilde{t}_1, \tilde{t}_2]^T$ and matrices $\mathbf{N}^v$, $\mathbf{N}^p$ store the interpolation functions for the velocity and pressure fields respectively.

The format presented above presume that the nodal components u_1 of velocity are numbered prior to components u_2, and both with the same nodal order.

REFERENCES

1. C.W. Hirt, A.A. Amsden and H.K. Cook, 'An arbitrary Lagrangian–Eulerian computing method for all flow speeds', *J. Comput. Phys.*, **14**, 227–253 (1974).
2. J. Donea, S. Giuliani and J.P. Halleux, 'An arbitrary Lagrangian–Eulerian finite element method for transient dynamic fluid–structure interactions', *Comput. Methods Appl. Mech. Eng.*, **33**, 689–723 (1982).
3. B. Ramaswamy and M. Kawahara, 'Arbitrary Lagrangian–Eulerian finite element method for unsteady, convective, incompressible viscous free surface fluid flow', *Int. J. Numer. Methods Fluids.*, **7**, 1053–1075 (1987).
4. T. Nomura and T. Hughes, 'An arbitrary Lagrangian–Eulerian finite element method for interaction of fluid and a rigid body', *Comput. Methods Appl. Mech. Eng.*, **95**, 115–138 (1992).
5. T. Nomura, 'A numerical study on vortex-excited oscillations of bluff cylinders', *J. Wind Eng. Ind. Aerodyn.*, **50**, 75–84 (1993).
6. C. Farhat, M. Lesoinne and N. Maman, 'Mixed explicit/implicit time integration of coupled aeroelastic problems: Three-field formulation, geometric conservation and distributed solution', *Int. J. Numer. Methods Fluids.*, **21**, 807–835 (1995).
7. R. Wei, A. Sekine and M. Shimura, 'Numerical analysis of 2D vortex-induced oscillations of a circular cylinder', *Int. J. Numer. Methods Fluids*, **21**, 993–1005 (1995).
8. S. Hurlbut, M. Spaulding and F. White, 'Numerical solution for laminar two-dimensional flow about a cylinder oscillating in a uniform stream', *J. Fluids Eng. ASME*, **104**, 214–220 (1982).
9. R. Chilukuri, 'Incompressible laminar flow past a transversely vibrating cylinder', *J. Fluids Eng. ASME*, **109**, 166–171 (1987).
10. Y. Lecointe and Y. Piquet, 'Flow structure in the wake of an oscillating cylinder', *J. Fluids Eng. ASME*, **111**, 139–148 (1989).
11. S. Mittal and T.E. Tezduyar, 'A finite element study of incompressible flows past oscillating cylinders and aerofoils', *Int. J. Numer. Methods Fluids.*, **15**, 1073–1118 (1992).
12. J. Zhang and C. Dalton, 'Interaction of a steady approach flow and a circular cylinder undergoing forced oscillation', *J. Fluids Eng. ASME*, **119**, 808–813 (1997).
13. P.M. Mendes, 'Numerical modelling of the aerodynamic behaviour of slender structures', *Ph.D. Thesis*, IST, Technical University of Lisbon, 1994 (in Portuguese).
14. O.C. Zienkiewicz, J. Szmelter and J. Peraire, 'Compressible and incompressible flow: an algorithm for all seasons', *Comput. Methods Appl. Mech. Eng.*, **78**, 105–121 (1990).
15. J. Donea, 'A Taylor–Galerkin method for convective transport problems', *Int. J. Numer. Methods Eng.*, **20**, 101–119 (1984).

16. P. Mendes and F. Branco, 'Numerical wind studies for the Vasco da Gama Bridge', *Struct. Eng. Int.*, **8**, 124–128 (1998).
17. O.C. Zienkiewicz and R. Taylor, *The Finite Element Method*, 4th edn, McGraw-Hill, London, 1991.
18. A.N. Brooks and T.J. Hughes, 'Streamline upwind Petrov–Galerkin formulations for convection dominated flows with particular emphasis on the incompressible Navier–Stokes equations', *Comput. Methods Appl. Mech. Eng.*, **32**, 199–259 (1982).
19. P.M. Gresho, S. Chan, R.L. Lee and C. Upson, 'A modified finite element method for solving the time-dependent incompressible Navier–Stokes equations. Part 1: Theory', *Int. J. Numer. Methods Fluids*, **4**, 557–598 (1984).
20. P.M. Gresho, 'Some current CFD issues relevant to the incompressible Navier–Stokes equations', *Comput. Methods Appl. Mech. Eng.*, **87**, 201–252 (1991).
21. P.M. Gresho, R.L. Lee and R.L. Sani, 'On the time-dependent solution of the incompressible Navier–Stokes equations in two and three dimensions', in C. Taylor and K. Morgan (eds.), *Recent Advances in Numerical Methods in Fluids*, Pineridge Press, Swansea, 1980.
22. P.M. Gresho, 'On the theory of semi-implicite projection methods for viscous incompressible flow and its implementation via a finite element method that also introduces a nearly consistent matrix. Part I—Theory', *Int. J. Numer. Methods Fluids*, **11**, 587–620 (1990).
23. A. Okajima, 'Numerical simulation of flow around rectangular cylinders', *J. Wind Eng. Ind. Aerodyn.*, **33**, 171–180 (1990).
24. G. Comini and S. Giudice, 'Finite element solution of the incompressible Navier–Stokes equations', *Numer. Heat Transf.*, **5**, 463–478 (1982).
25. T. Tamura and K. Kuwahara, 'Numerical study of aerodynamic behavior of a square cylinder', *J. Wind Eng. Ind. Aerodyn.*, **33**, 161–170 (1990).
26. C. Song and M. Yuan, 'Simulation of vortex-shedding flow about a circular cylinder at high Reynolds numbers', *J. Fluids Eng. ASME*, **112**, 155–161 (1990).
27. R. Scanlan, 'Wind dynamics of longspan bridges', in A. Larsen (ed.), *Aerodynamics of Large Bridges*, Balkema, Rotterdam, 1992.
28. G. Karniadakis and G. Triantafyllou, 'Three-dimensional dynamics and transition to turbulence in the wake of bluff objects', *J. Fluid Mech.*, **238**, 1–30 (1992).
29. S. Jordan and J. Fromm, 'Oscillatory drag, lift and torque on a circular cylinder in a uniform flow', *Phys. Fluids.* **15**, 371–380 (1972).
30. J. Sa and K. Chang, 'Shedding patterns of the near-wake vortices behind a circular cylinder', *Int. J. Numer. Methods Fluids*, **12**, 463–474 (1991).
31. A. Roshko, 'Experiments on the flow past a circular cylinder at very high Reynolds number', *J. Fluid Mech.*, **10**, 345–356 (1961).
32. C. Williamson, 'Defining a universal and continuous Strouhal–Reynolds number relationship for the malinar vortex shedding of a circular cylinder', *Phys. Fluids.* **31**, 2742–2744 (1988).
33. M. Braza, P. Chassaing and H. HaMinh, 'Numerical study and physical analysis of the pressure and velocity fields in the near wake of a circular cylinder', *J. Fluid Mech.*, **165**, 79–130 (1986).
34. R. Franke, W. Rodi and B. Schonung, 'Numerical calculation of laminar vortex-shedding flow past cylinders', *J. Wind Eng. Ind. Aerodyn.*, **35**, 237–257 (1990).
35. Y. Lecointe and J. Piquet, 'On the use of several compact methods for the study of unsteady incompressible viscous flow round a circular cylinder', *Comput. Fluids*, **12**, 255–280 (1984).
36. Y. Tanida, A. Okajima and Y. Watanabe, 'Stability of a circular cylinder oscillating in uniform flow or in a wake', *J. Fluid Mech.*, **61**, 769–784 (1973).
37. G. Koopmann, 'The vortex wakes of vibrating cylinders at low Reynolds numbers', *J. Fluid Mech.*, **28**, 501–512 (1967).
38. O. Griffin and S. Ramberg, 'The vortex wakes of vibrating cylinders at low Reynolds numbers', *J. Fluid Mech.*, **66**, 553–576 (1974).
39. A. Okajima, T. Nagahisa and A. Rokugoh, 'A numerical analysis of flow around rectangular cylinders', *JSME Int. J. Series II*, **33**, 702–711 (1990).
40. A. Okajima, H. Ueno and H. Sakai, 'Numerical simulation of laminar and turbulent flows around rectangular cylinders', *Int. J. Numer. Methods Fluids.*, **14**, 999–1012 (1992).
41. Y. Nakamura and Y. Yoshimura, 'Flutter and vortex excitation of rectangular prisms in pure torsion in smooth and turbulent flows', *J. Sound Vibr.*, **84**, 305–317 (1982).
42. K. Washizu, A. Ohya, Y. Otsuki and K. Fujii, 'Aeroelastic instability of rectangular cylinders in a torsional mode due to a transverse wind', *J. Sound Vibr.*, **72**, 507–521 (1980).
43. Y. Nakamura, 'On the aerodynamic mechanism of torsional flutter on bluff structures', *J. Sound Vibr.*, **67**,163–177 (1979).
44. D. Huston, 'Flutter derivatives from 14 Generic deck sections', *Bridges and Transmission Line Structures. Proc. of the 1987 ASCE Structures Congress*, Orlando, USA, 1987.
45. K. Washizu, A. Ohya, Y. Otsuki and K. Fujii, 'Aeroelastic instability of rectangular cylinders in a heaving mode', *J. Sound Vibr.*, **59**, 195–210 (1978).
46. Y. Nakamura and T. Mizota, 'Unsteady lifts and wakes of oscillating rectangular prisms', *J. Eng. Mech. Div. ASCE*, **101**, 855–871 (1975).
47. L. Shangpei, and C. Xin, 'Experimental identification of flutter derivatives from several typical deck sections', in *Recent Advances in Wind Engineering*, Pergamon Press, London, 1989, pp. 610–617.

